Available online at www.sciencedirect.com
ScienceDirect
Trans. Nonferrous Met. Soc. China 34(2024) 4020−4031
Transactions of Nonferrous Metals Society of China
www.tnmsc.cn

# Improvement of crystal structure and electrical performance of NASICON-type $NaTi_2(PO_4)_3$ solid electrolyte by doping $Cr^{3+}$ ions

Cheng-jian WEN, Zhi-wei LUO, Xin-yu LIU, Ju-xia TONG, Pan HE, An-xian LU

School of Materials Science and Engineering, Central South University, Changsha 410083, China

Received 22 April 2023; accepted 20 September 2023

**Abstract:** A series of $Cr^{3+}$-substituted $Na_{1+x}Ti_{2-x}Cr_xP_3O_{12}$ ($x$=0.1, 0.2, 0.3, 0.4, 0.5, molar fraction) solid electrolytes were prepared by the solid-phase reaction method. The effects of $Cr^{3+}$ ions on the phase composition, microstructure, and electrochemical ion conductivity of Na-based conductors were studied using X-ray powder diffraction, field emission scanning electron microscopy, and AC impedance measurement. The results show that the main crystal phase of $NaTi_2(PO_4)_3$ is formed in the solid electrolytes. The substitution of $Ti^{4+}$ sites by 15 at.% $Cr^{3+}$ ions contributes to the enhancement of electrical conductivity, which is attributed to the combined effect of suppressing the formation of impurity phases, broadening ion channels, and improving the bonding degree of grains. $Na_{1.3}Ti_{1.7}Cr_{0.3}P_3O_{12}$ electrolyte can obtain the best ionic conductivity of $6.13\times10^{-6}$ S/cm at room temperature, which is 8 times that of the undoped $NaTi_2(PO_4)_3$ electrolyte.

**Key words:** $NaTi_2(PO_4)_3$; solid electrolyte; crystal structure; ionic conductivity; Cr-doping

## 1 Introduction

All-solid-state sodium-ion batteries are considered to be the most promising energy storage devices to replace liquid batteries due to their lower cost, longer cycle life and higher energy density, showing great potential for applications in new energy electric vehicles, portable microelectronic devices and other fields [1−3]. As the core part of all-solid-state sodium-ion batteries, it is crucial to design and develop a solid-state electrolyte with good performance [1]. At present, the reported sodium ion solid electrolytes mainly include $\beta$/$\beta''$-$Al_2O_3$, sodium sulfide system, and NASICON system. Of these, $\beta$/$\beta''$-$Al_2O_3$ exhibits ionic conductivity comparable to that of liquid electrolytes but requires an environment above 300 °C for stable operation [4,5]. The sodium-based sulfur-based electrolyte has poor stability (chemical stability and interface problems) and needs to be handled in an inert environment during processing. In addition, the requirements for the selection of electrode materials and reagents when making battery modules are more stringent. Therefore, sulfides as conductive materials are less suitable for large-scale commercial development [6,7]. NASICON-type compounds are the most widely studied ion-conducting media at this stage and are considered to be the most potential application materials due to their high bulk ionic conductivity and good air stability [8].

The general formula of NASICON structure is $AB_2(MO_4)_3$ (A = Li/Na/K, B = Zr/Ti/Ge/Sn, M = Si/P) [9,10]. Among them, the $Na_3Zr_2Si_2PO_{12}$ (NZSP) based system has made great progress and has shown good ionic conductivity properties [11]. However, $NaTi_2(PO_4)_3$ (NTP) compounds and their associated solid solutions, which also possess a 3D conduction pathway, have been less well studied.

**Corresponding author:** Zhi-wei LUO, Tel: +86-731-88877057, E-mail: loaswell@163.com
DOI: 10.1016/S1003-6326(24)66655-0

NTP is a rhombohedral crystal system ($R\bar{3}c$). Structurally, it consists of $TiO_6$ octahedra and $PO_4$ tetrahedra arranged by cross-linking each other using co-apex angles, producing a three-dimensional rigid channel with $[Ti_2(PO_4)_3]$ as the backbone. While $Na^+$ is distributed along the *c*-axis in a $TiO_6$—Na—$TiO_6$ band structure [12,13]. When migrating, the carriers achieve rapid diffusion by hopping continuously by overcoming the force of the polyanion backbone. However, the conduction effect of pure NTP in practical research is not ideal.

So far, only a few literatures have attempted to analyze the ionic conduction phenomenon, and the purpose of enhancing the system's performance has been achieved mainly by ion doping or by changing the technical route of the synthesis process. NIETO-MUÑOZ et al [14] synthesized Al-doped NTP conductive glass-ceramics by controlling the crystallization of the parent glass by heat treatment. The electrical conductivity of the material is effectively improved by this method, and the ionic conductivity can reach $3.4\times10^{-3}$ S/cm at 300 °C. However, the melting process of the raw material requires high temperatures of up to 1450 °C. In addition, to ensure the uniformity of the composition, the melting and cooling must be repeated, so the experimental process is cumbersome and technically difficult. As we all know, the solid-phase reaction is a relatively simple preparation process. MOUAHID et al [15] prepared $Na_{1+x}Al_xTi_{2-x}(PO_4)_3$ $(0.4\leq x\leq 0.9)$ inorganic solid electrolytes at a relatively low temperature (725 °C) by solid-phase reaction method. It was found that the ionic conductivity at room temperature increased with the increase of the $Al^{3+}$ doping amount. This is explained by the author [15], who suggests that this change in electrical property is caused by an increase in carrier concentration in the matrix. It is worth noting that although the solid solubility of $Al^{3+}$ can reach 0.9 mol, the ionic conductivity of the sample at room temperature is only $1.3\times10^{-7}$ S/cm, which indicates that the geometric factor of the ion migration channel still needs to be considered. When $Ti^{4+}$ (0.0605 nm) is replaced by $Al^{3+}$ (0.0535 nm) with a smaller radius, the transport of $Na^+$ ions is constrained by the reduction in the size of the bottleneck in the diffusion channel, and thus the conductivity does not increase significantly.

The purpose of this work is to design and synthesize NTP solid-state electrolytes with higher ionic conductivity by controlling structural defects. In this work, $Cr^{3+}$ is selected as the performance modifier of NTP. $Cr^{3+}$ ions are used to replace $Ti^{4+}$ ions in the structure, and the crystal structure diagram is shown in Fig. 1, forming structural defects and introducing excess $Na^+$ balance charge, thereby improving the conductivity of NTP. The relevant defect reaction formula is shown in Eq. (1):

$$Cr_2O_3+2Ti_{Ti}^{*}+8Na_{Na}^{*}\rightarrow 2Cr_{Ti}'+2Na^{\cdot}+3Na_2O \quad (1)$$

In addition, when $Cr^{3+}$ (0.0615 nm) with a larger radius replaces $Ti^{4+}$ (0.0605 nm) with a smaller radius in the structure, the ion migration channel can be broadened, and it is expected to further improve the ionic conductivity. Therefore, NASICON-type NTP materials with different Cr contents were prepared by the solid-state reaction method, and the effects of doping concentration and sintering behavior on the crystal structure, micromorphology, and electrical conductivity were studied.

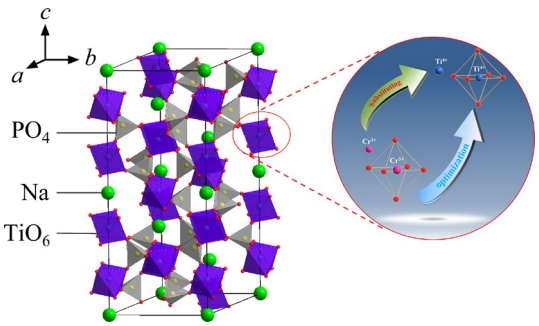


**Fig. 1** Crystal structure of $NaTi_2(PO_4)_3$ and schematic diagram of substitution of $Cr^{3+}$ for $Ti^{4+}$ site

## 2 Experimental

### 2.1 Preparation of materials

$Cr^{3+}$-doped NASICON-type NTP electrolytes were prepared by solid-phase sintering in an air environment. Chemical reagent grades $Cr_2O_3$ (Sinopharm Chemical Reagent Co., Ltd., 99%), $Na_2CO_3$ (Sinopharm Chemical Reagent Co., Ltd., 99.99%), $TiO_2$ (Xilong Scientific Co., Ltd., 99.5%), and $NH_4H_2PO_4$ (Sinopharm Chemical Reagent Co., Ltd., 99.5%) were selected as the raw materials of the samples, they were according to the chemical formula $Na_{1+x}Ti_{2-x}Cr_xP_3O_{12}$(NTCP, $x$ =0.1, 0.2, 0.3, 0.4, 0.5, in molar fraction) in the corresponding molar ratio to participate in the reaction. For the

convenience of differentiation, the components with different $Cr^{3+}$ contents are marked as C1, C2, C3, C4, and C5, respectively. The weighed raw materials were transferred to a high-energy ball mill, and they were homogenized with ethanol as a dispersant at 400 r/min for 4 h, to obtain active particles with uniform mixing and high specific surface area. The ball-milled wet material was fully dried at 80 °C in a blast drying oven, and then moved into a corundum crucible for pre-sintering at 550 °C for 10 h (to completely separate volatile components), and cooled with the furnace. The material cooled to room temperature was ball-milled again for 6 h and dried at 80 °C to obtain the NTCP precursor in a fine state. In the molding stage, polyvinyl alcohol (PVA) as a binder was placed in an agate mortar and finely ground by hand together with the precursor powder, and the granulated mixed powder was pressed into a 12 mm-diameter disc with a uniaxial pressure of 25 MPa. Finally, the discs were held at 750−850 °C for 10 h to complete the dense sintering. The heating rates used were all 3 °C/min.

## 2.2 Characterization

2.2.1 XRD

The XRD patterns of the samples were recorded by a D/max2500 Cu target ($\lambda$=1.541 Å) X-ray diffractometer. The specific chemical composition of the obtained data was initially searched and identified in the Jade 6.0 analysis software, and then the refinement of lattice parameters and the acquisition of phase quantitative analysis information was completed through the Tops-Academic program.

2.2.2 XPS

The composition and electronic state of the elements in the samples were measured by Thermo Scientific X-ray Photoelectron Spectrometer (XPS), and the binding energies of the elements were corrected using the energy standard of 284.80 eV C1s.

2.2.3 FTIR

To further identify the structure of the sample, reasoning and verification should be carried out according to the position and shape of the absorption peak in the infrared spectrum. The powder of the sintered sample and the KBr filler were mixed at a mass ratio of 1:100, pressed into tablets, and then the flake samples were transferred to a Fourier transform infrared spectrometer (Nicolet Smart) for structural information collection, and the range of wavenumber recording was selected to be 400−4000 $cm^{-1}$.

2.2.4 SEM

A field emission electron microscope (FESEM, SIRION200) was used to collect the microstructure and morphology of the section, and the distribution and content of related elements were qualitatively and semi-quantitatively detected by the equipped X-ray energy dispersive spectrometer (EDS).

2.2.5 Density measurement

To obtain the change law of the density of the material after sintering, the apparent density of the sample was measured by the Archimedes drainage method, and the specific value was calculated according to Formula (2):

$$\rho_a = \frac{m_1}{m_1 - m_2} \times \rho_l \tag{2}$$

where $\rho_a$ is the apparent density, $\rho_l$ is the density of the suspension medium (ethanol is selected, 0.79 $g/cm^3$), $m_1$ is the dry mass in the air, and $m_2$ is the mass of the alcohol.

2.2.6 EIS

The AC impedance of the solid electrolyte was measured by a UTOLAB electrochemical workstation (Metrohm, Switzerland, M204). Before testing, the sintered samples were polished to optical grade with SiC sandpaper. After the corresponding geometries were measured, the parallel surfaces of the samples were coated with a silver paste for the formation of blocking electrodes. At room temperature, a small amplitude sinusoidal disturbance signal of 50 mV was applied to the electrode system (the frequency range was set to be (50−0.5)×$10^6$ Hz). The AC impedance information can be obtained from the response relationship between the electrode and the disturbance voltage. Finally, the Z-View software was used for nonlinear fitting of the original impedance data, obtaining the corresponding impedance, and converting the conductivity ($\sigma$) of the sample according to Formula (3):

$$\sigma = l/(Rs) \tag{3}$$

where $R$ is the impedance (Ω), $l$ is the thickness (cm), and $s$ is the electrode area ($cm^2$).

## 3 Results and discussion

### 3.1 Phase composition

The X-ray diffraction patterns of all the samples sintered at 800 °C for 10 h are shown in Fig. 2(a). The results show that the main NASICON-type $NaTi_2(PO_4)_3$ crystal phase was successfully synthesized under this sintering condition, and its space group is $R\bar{3}c$, $a \approx 8.49$ Å, and $c \approx 21.79$ Å. When the Cr doping content is small ($x = 0.1$), it is accompanied by the formation of the impurity phase $TiP_2O_7$, while the Samples C2, C3 and C4 do not contain impurity peaks. When the Cr element continues to increase ($x = 0.5$), the characteristic diffraction corresponding to $CrPO_4$ begins to appear. According to our previous study [16], the formation of the $TiP_2O_7$ impurity phase is caused by the volatilization of the Na element during the high-temperature sintering of the undoped NTP. In the NTCP, the substitution of $Ti^{4+}$ ions by $Cr^{3+}$ ions will introduce more Na elements to maintain electrical neutrality, and the $TiP_2O_7$ impurity phase can be further converted into the $NaTi_2(PO_4)_3$ conductive crystal phase by the supplemented Na elements. In addition, when the Cr content exceeds 0.4, the secondary phase $CrPO_4$ is easier to form. For this reason, the Cr content should be controlled within a certain range.

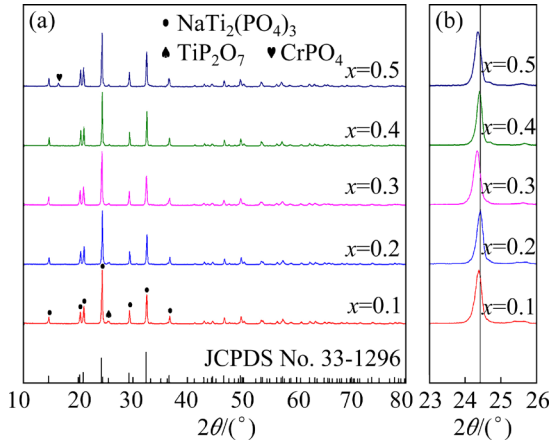


**Fig. 2** XRD patterns of $Na_{1+x}Ti_{2-x}Cr_x(PO_4)_3$ obtained after sintering at 800 °C (a) and enlarged XRD patterns at $2\theta$ values of 23°−26° (b)

The local magnification of the strongest diffraction peak of the main crystal phase in NTCP is shown in Fig. 2(b). The characteristic peak position at the diffraction angle of 24.4° is slightly shifted to lower angles by doping $Cr^{3+}$. According to the Bragg's equation: $2d\sin\theta=n\lambda$, the corresponding $d$ value increases when $\theta$ decreases, indicating that the distance between atomic lattices in the crystal structure is widened. This is attributed to the fact that the ionic radius of $Cr^{3+}$ (0.0615 nm) is slightly larger than that of $Ti^{4+}$ (0.0605 nm) so that the substitution of the Ti element for Cr can widen the distance between atomic sites. The XRD data of the samples were refined and fitted using the Rietveld method to visualize the change in the crystal structure more intuitively. Figure 3 shows the fitting results for Sample C3, and the specific values are listed in Table 1. It can be found that the unit cell parameters of the sample are enlarged with the increase in $Cr^{3+}$ concentration, from $a = 8.4900$ Å and $c = 21.794$ Å in Sample C1 to $a = 8.5013$ Å and $c = 21.835$ Å in Sample C3. When the doping content increases to a certain level ($x > 0.3$), the unit cell parameters begin to decrease, which indicates the distortion of the crystal structure caused by excessive $Cr^{3+}$ doping. Therefore, it can be deduced that the optimal Cr doping amount of the NASICON-type $Na_{1+x}Ti_{2-x}Cr_x(PO_4)_3$ is 0.3 based on the variation trend of the unit cell parameters.

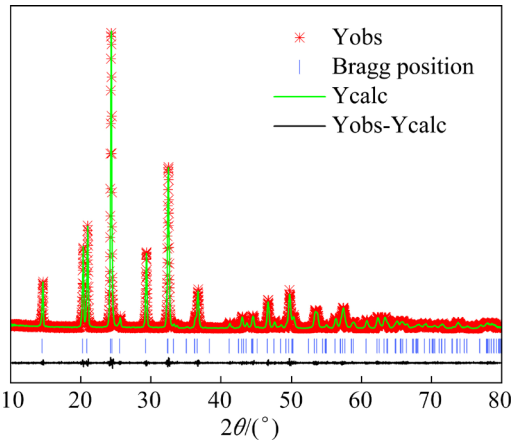


**Fig. 3** XRD Rietveld refinement results of Sample C3

**Table 1** Cell parameters for $Na_{1+x}Ti_{2-x}Cr_x(PO_4)_3$ from Rietveld fitting

| Sample | $a$ (=$b$)/Å | $c$/Å | $V$/Å$^3$ | $R_{wp}$/% |
|---|---|---|---|---|
| C1 ($x$=0.1) | 8.4900(5) | 21.794(2) | 1360.4(2) | 9.68 |
| C2 ($x$=0.2) | 8.4981(3) | 21.805(1) | 1363.8(1) | 9.51 |
| C3 ($x$=0.3) | 8.5013(4) | 21.835(2) | 1366.7(2) | 9.62 |
| C4 ($x$=0.4) | 8.5327(3) | 21.803(1) | 1374.7(1) | 9.72 |
| C5 ($x$=0.5) | 8.5183(1) | 21.775(4) | 1368.4(4) | 9.64 |

To study the effect of sintering temperature on the phase composition and unit cell parameters of Sample C3 obtained at different sintering temperatures, they were selected for X-ray diffraction analysis at room temperature. The XRD patterns are shown in Fig. 4, the pure $NaTi_2(PO_4)_3$ crystal phase can be obtained when the sintering temperature is higher than 800 °C, and the impurity phase $Cr_5(P_3O_{10})_3$ (PDF#31-0411) will be formed below this temperature. Therefore, the subsequent performance characterization analysis was mainly carried out on the NTCP samples obtained by sintering at 800 °C. In addition, the Rietveld fitting results of the samples with different Cr doping contents and different sintering temperatures are presented in Figs. 5(a) and (b), respectively. It can be seen from the figure that the unit cell parameters of the NTCP samples first increase and then decrease with the doping of the Cr element, but remain unchanged with the increase of the sintering temperature. This change rule shows that the crystal structure is less affected by the sintering temperature, but is greatly affected by $Cr^{3+}$. The increase of unit cell parameters and the acquisition of channels more favorable for the migration of sodium ions is achieved by the substitution of $Cr^{3+}$ for $Ti^{4+}$.

### 3.2 X-ray photoelectron spectroscopy

The XPS spectrum of NTCP is shown in Fig. 6(a), where C 1s with a binding energy of

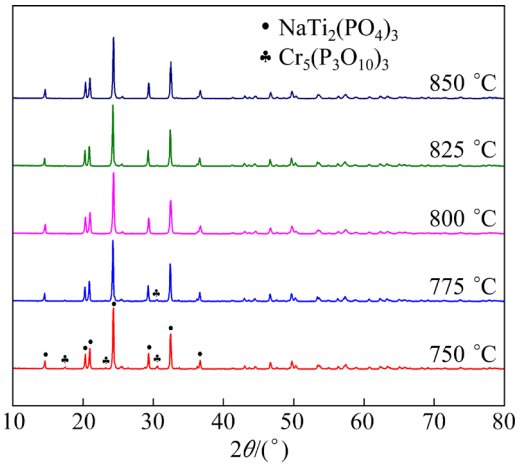


**Fig. 4** XRD patterns of Sample C3 obtained after sintering at different temperatures

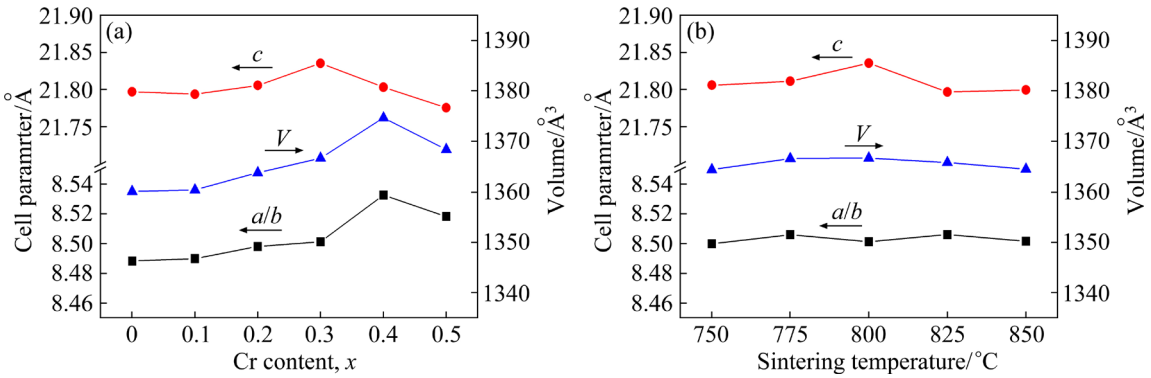


**Fig. 5** Evolution of cell parameter and unit cell volumes for $Na_{1+x}Ti_{2-x}Cr_x(PO_4)_3$ with Cr doping content (a) and sintering temperature (b)

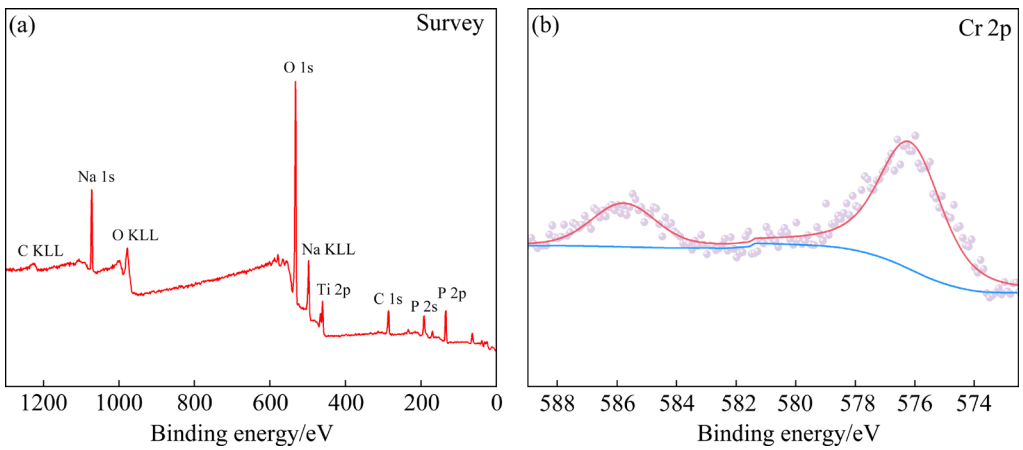


**Fig. 6** XPS spectrum of each element of Sample C3 (a) and high-resolution fine spectrum of Cr 2p (b)

284.8 eV was used for spectral calibration. It can be found that the characteristic peaks of Na1s, Ti 2p, P 2p, P 2s, and O 1s are presented in the whole spectrum, which indicates that the elements Na, Ti, P, and O are mainly contained in the sample [17]. Due to the low content of Cr in the matrix, its electronic state cannot be observed in the full spectrum, so it must be refined. A partially enlarged view of the doping element Cr 2p ($Na_{1.3}Ti_{1.7}Cr_{0.3}P_3O_{12}$) is shown in Fig. 6(b). It is specifically composed of doublets with binding energies of 576.3 and 585.8 eV, corresponding to the spin-orbit doublets of $2p_{3/2}$ and $2p_{1/2}$, respectively [18], indicating that the $Cr^{3+}$ ion has successfully entered the NASICON lattice.

### 3.3 Infrared spectroscopy

Infrared spectroscopy is considered to be an effective test method to explore the ionic bonding state of materials, which can understand the vibrational characteristics of the corresponding functional group chemical bonds through peak positions in different regions. The FTIR spectra of the NTCP samples obtained after sintering at 800 °C for 10 h are shown in Fig. 7. To better understand the structural changes of the solid electrolyte samples, the FTIR data of the undoped NTP in the earlier work were used for comparison. It can be seen from the infrared spectrum that the infrared absorption characteristics of all components are generally similar in the test range of 4000−400 $cm^{-1}$. The corresponding absorption peaks of the samples mainly appear in the following wavenumber ranges: 3440−3446, 1630−1638, 1223−1227, 1023−1039, 639−642 and 568−573 $cm^{-1}$. Combined with the relevant literature [19−21], it can be seen that the absorption in the 3440−3446 and 1630−1638 $cm^{-1}$ bands mainly corresponds to the bending vibration modes of the P—O—H or H—O—H bonds, which are caused by the hygroscopic properties of the phosphate matrix itself and the moisture mixed by the KBr press method during the test.

The rhombohedral $NaTi_2(PO_4)_3$ is composed of $[TiO_6]$ octahedra and $[PO_4]$ tetrahedra connected by corner-sharing to form a three-dimensional framework. The absorption characteristics of inorganic materials in the infrared region are generally caused by the lattice vibrations of the anions (clusters), so the absorption bands in the 1300−400 $cm^{-1}$ range mainly originate from the infrared absorption properties of the $[TiO_6]$ and $[PO_4]$ atomic groups. By consulting the literature, the vibration modes of chemical bonds corresponding to each characteristic absorption band are summarized in Table 2. The absorption band in the wavelength range of 1223−1227 $cm^{-1}$ corresponds to the asymmetric stretching vibration of the O—P—O bond; the broader strong vibrational absorption feature peak at 1023− 1039 $cm^{-1}$ is attributed to symmetric stretching vibrations induced by $PO_4^{3-}$ tetrahedra [22]; the absorption peak in the range of 639−642 $cm^{-1}$ is related to the stretching vibration mode caused by the Ti—O—P bond [23,24]; the band near 568−573 $cm^{-1}$ is due to the flexural vibration absorption of O—P—O bonds [23].

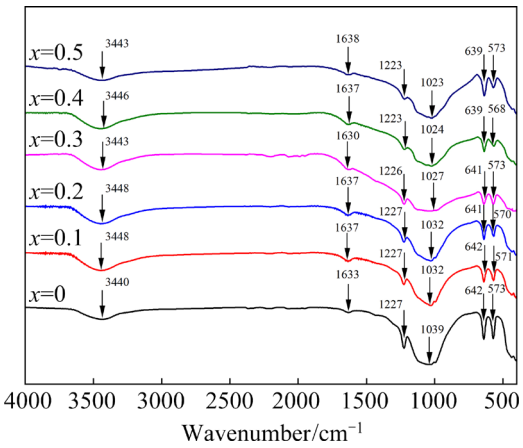


**Fig. 7** FTIR spectra of $Na_{1+x}Ti_{2-x}Cr_x(PO_4)_3$ solid electrolyte obtained after sintering at 800 °C

**Table 2** Vibration types corresponding to infrared spectrum of NTCP ceramics

| Absorption frequency/$cm^{-1}$ | Vibration type |
|---|---|
| 3440−3446 | Bending vibration of P—O—H bond |
| 1630−1638 | Bending vibration of H—O—H bond |
| 1223−1227 | Asymmetric stretching vibration of O—P—O bond |
| 1023−1039 | Symmetric stretching vibration of $PO_4^{3-}$ tetrahedron |
| 639−642 | Stretching vibration of Ti—O—P bond |
| 568−573 | Bending vibration of O—P—O bond |

It is noteworthy that as the Cr doping content increases, a tendency for the IR absorption peaks to shift slightly towards the lower wavenumbers is observed near the 1223−1227, 1023−1039, and

639−642 $cm^{-1}$. This is attributed to the substitution of the smaller atomic number of Ti element (atomic number 22) by the larger atomic number of Cr element (atomic number 24) in the anion group. In addition, the corresponding infrared absorption peaks in the wavelength range of 639−642 $cm^{-1}$ were enhanced with the increase of doping content. In particular, the absorption band in the C5 component appears more prominently through the precipitation of the impurity phase $CrPO_4$. It is speculated that the absorption behavior in this band range is represented by the relevant vibrational modes of the Cr—O—P bond. The successful substitution of $Cr^{3+}$ for $Ti^{4+}$ in the NASICON structure is explained by the evolution law of the unit cell parameters of NTCP and the change in the Fourier transform infrared spectrum.

### 3.4 Microscopic topography

To study the crystallization behavior, grain size, and porosity of NTCP components, the secondary electron images of the fracture surface of the sintered samples were obtained by scanning electron microscopy. The microstructures of the samples with different Cr contents after sintering at 800 °C for 10 h are shown in Fig. 8. The main crystal phase in NTCP is irregular polygonal grains with an average grain size of about 1 μm. Among them, the grain size in Sample C1 varies. Combined with the phase search results of the XRD data, it can be seen that the existence of more small grains in the composition is caused by that of the impurity phase $TiP_2O_7$. Similarly, there is a clear size difference in the overall grain size caused by the presence of the secondary phase $CrPO_4$ in Sample C5.

From the SEM images of Samples C1 to C5, the pores inside the samples are effectively reduced, the degree of bonding between grains is increased, and the phenomenon that the packing of grains becomes more compact is observed by Cr doping. The densest grain distribution morphology of the cross-section is presented when the doping content is 0.3. The hindrance in the Na ion conduction process is reduced by this optimized microstructure so that the ionic conductivity of the NTCP electrolytes is advantageously improved. Based on the above SEM characterization analysis, the doping of an appropriate amount of Cr element, on the one hand, the formation of impurity phases in the NASICON-type solid electrolyte can be suppressed, on the other hand, the density of the sample can be effectively improved, and the sintering performance can be improved. The EDS analysis results of Sample C3 are shown in Figs. 8($c_1$−$c_5$). It can be seen that Na, Ti, Cr, P, and O are uniformly distributed without obvious segregation behavior. It further shows that the doping elements have been successfully incorporated into the lattice, which is consistent with the characterization results obtained by XRD, XPS, and IR.

The surface of the NTCP system and the density data obtained by the Archimedes method are shown in Fig. 9. The surface of NTCP is light green due to Cr doping, it deepens with the increase of its content, and the corresponding shrinkage degree also increases, indicating that its density has been improved. When the dosage reaches 0.5, the surface of the sample is transformed into a yellow-green color. Combined with the XRD results, the chromium impurity phase is precipitated. In addition, the variation trend of the apparent density of NTCP is presented in the figure. The corresponding densities of the NTCP electrolytes after sintering at 800 °C for 10 h range from 2.861 to 2.907 $g/cm^3$. Obviously, with the increase of Cr doping content, the density of the sample is continuously improved. The microstructure analysis shows that the doping of an appropriate amount of Cr element can significantly reduce the pores introduced by the solid-phase sintering method, and the crystal particles are formed into a good packing shape, so the density of the NTCP is correspondingly improved.

### 3.5 Conductive properties

To study the effect of $Cr^{3+}$ doping on the electrical conductivity of the NTP system, the AC impedance spectrum of sample at room temperature was obtained by an electrochemical workstation, and the corresponding resistance was determined accordingly. According to the knowledge of the relevant complex impedance map, the Nyquist diagram is composed of the (grain + grain boundary) response of the arc part and the blocking electrode polarization response of the straight part. Therefore, the standard impedance map is generally represented as a geometric figure composed of two semicircles and an inclined straight line, where

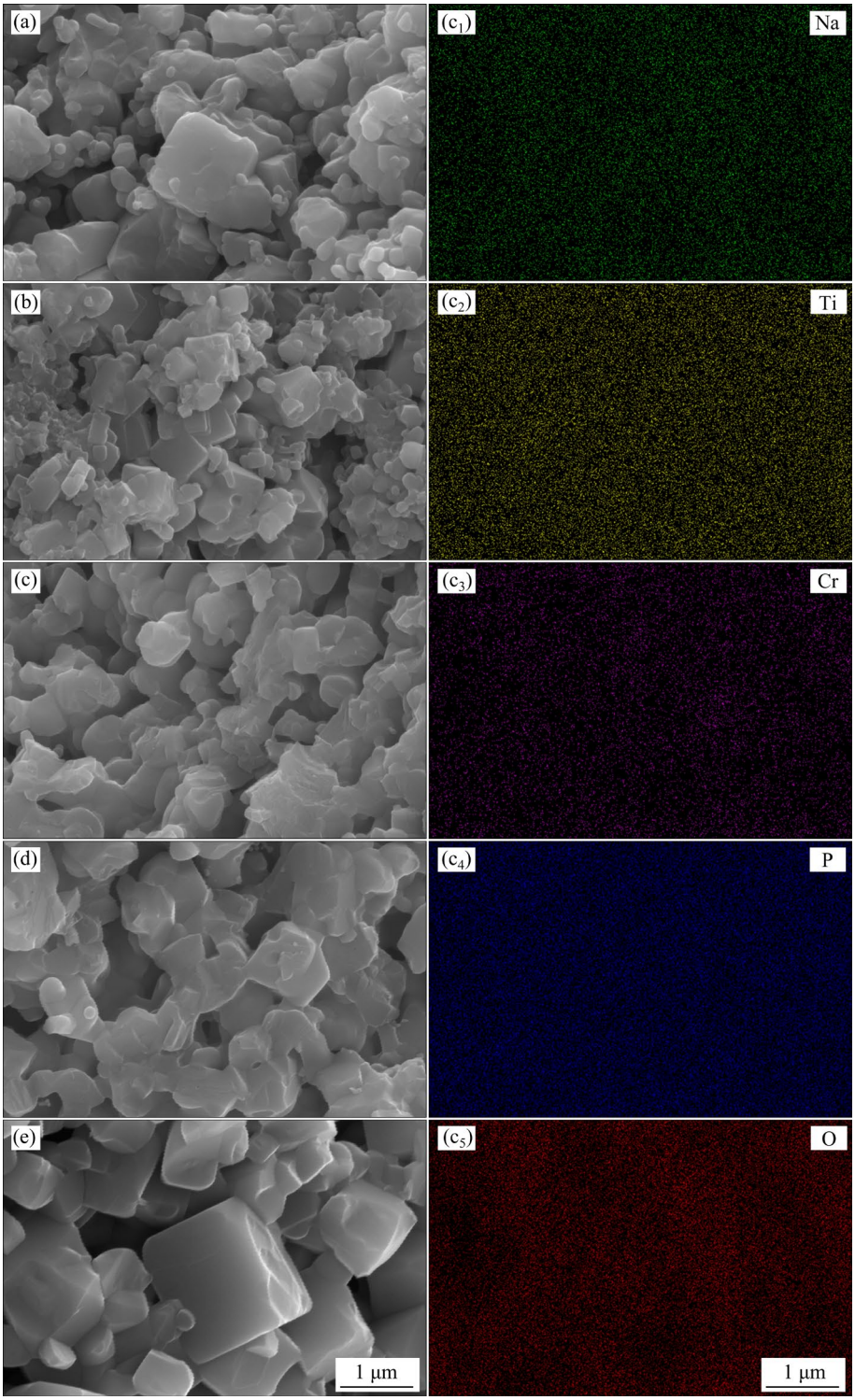


**Fig. 8** SEM fracture morphologies of Sample C1 (a), Sample C2 (b), Sample C3 (c), Sample C4 (d) and Sample C5 (e); Element distribution maps of Sample C3: ($c_1$) Na; ($c_2$) Ti; ($c_3$) Cr; ($c_4$) P; ($c_5$) O

the semicircle in the high-frequency region corresponds to the grain conduction and the size of its diameter represents the grain impedance; the semicircle in the intermediate frequency part is related to the ion transport at the grain boundary and the intercept at the right end of this arc represents the sum of the grain and grain boundary impedances. However, this experiment was limited by the operating frequency range, and no apparent grain impedance response was observed. Therefore, we only analyzed the total resistance of the NTCP samples.

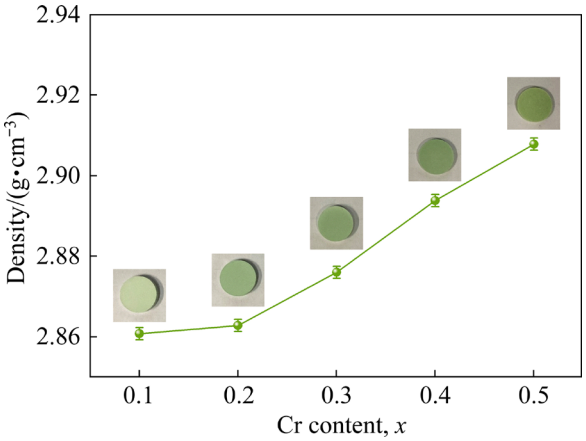


**Fig. 9** Density and photos of NTCP obtained after sintering at 800 °C

The impedance behaviors of NTCP electrolytes with different Cr doping contents obtained by sintering at 800 °C for 10 h are shown in Fig. 10(a). With the increase of Cr content, the corresponding impedance first decreased and then increased, indicating that the conductivity of this NASICON-type solid electrolyte was successfully improved by the doping of the Cr element. The related XRD data analysis shows that the precipitation of impurity phases in NTCP electrolytes can be avoided by doping with an appropriate amount of Cr element, so the adverse effects of these impurity phases on ionic conduction are reduced to a certain extent. On the one hand, the migration channel of sodium ions can be broadened due to the substitution of Cr for Ti, and more conductive sodium ions are introduced to maintain electrical neutrality. On the other hand, according to the micro-morphological analysis of the cross-section, the grain morphology of the NTCP sample can be densified by the doping of Cr element, which promotes the ion conduction efficiency.

Through calculation, the variation law of the conductivity of NTCP with the additional content of $Cr^{3+}$ is shown in Fig. 10(b). With the increase of $Cr^{3+}$ concentration, the corresponding ionic conductivity increased first and then decreased. The best room temperature ionic conductivity was obtained when the doping content was 0.3, which was $6.13\times10^{-6}$ S/cm. This value is 8 times that of undoped NTP. It is worth noting that the conductivity of the samples was significantly reduced when too much $Cr^{3+}$ ($x > 0.3$) was doped. The main reason for this sudden change in electrical

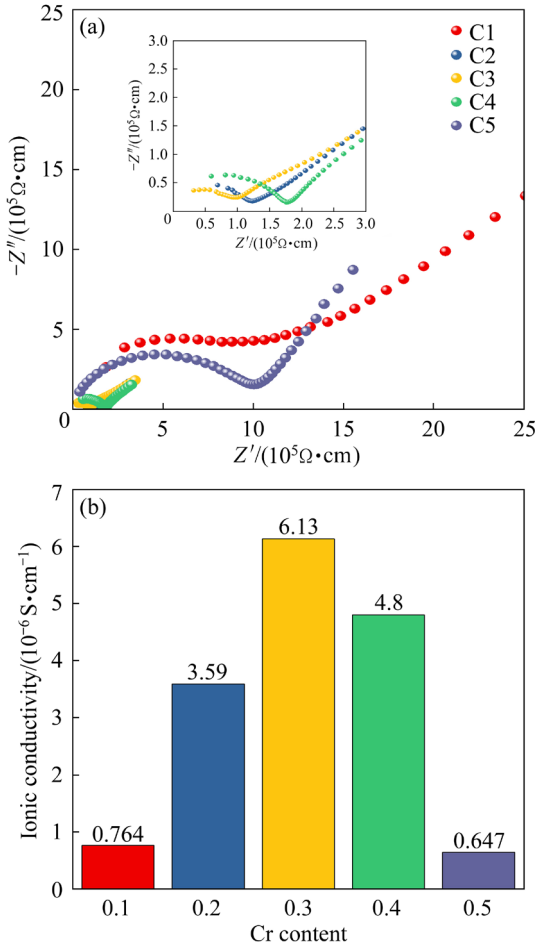


**Fig. 10** Impedance spectra (a) and corresponding ionic conductivity (b) of NTCP after sintering at 800 °C

properties is that the lattice is distorted due to the over-doping of foreign ions so that the NASICON-type structure suitable for carrier migration is disturbed. Similarly, $Na_{1+x}Al_xGe_{2-x}(PO_4)_3$ ($0 \le x \le 1.0$) glass-ceramic system was studied by ORTIZ-MOSQUERA et al [25]. The results show that the optimal conductivity of the NAGP component is obtained at $x = 0.8$. When the Al doping content is further increased, an excessive $AlPO_4$ impurity phase is formed and the structure is changed so that the ion conduction efficiency is affected. This phenomenon is consistent with the conclusion from NMR analysis [26].

To study the effect of sintering temperature on the ionic conductivity of NTCP, the electrochemical information presented by the C3 components obtained at different sintering temperatures was selected for comparison. The changes in impedance and ionic conductivity with sintering temperature are shown in Fig. 11. With the increase in sintering temperature, its ionic conductivity first increased

and then decreased, and the best performance was obtained at the preparation temperature of 800 °C. X-ray diffraction results show that the pure $NaTi_2(PO_4)_3$ phase can only be produced when the sintering temperature is above 800 °C, while the $Cr_5(P_3O_{10})_3$ impurity phase is easily precipitated at a lower sintering temperature. Combining the effects of different sintering temperatures on the microscopic morphology of $LiTi_2(PO_4)_3$, the abnormal growth of some crystals is caused by higher sintering temperatures, and cracks are more likely to be formed at the grain boundaries, thereby hindering ion conduction. Therefore, the conductivity decreases as the sintering temperature continues to increase.

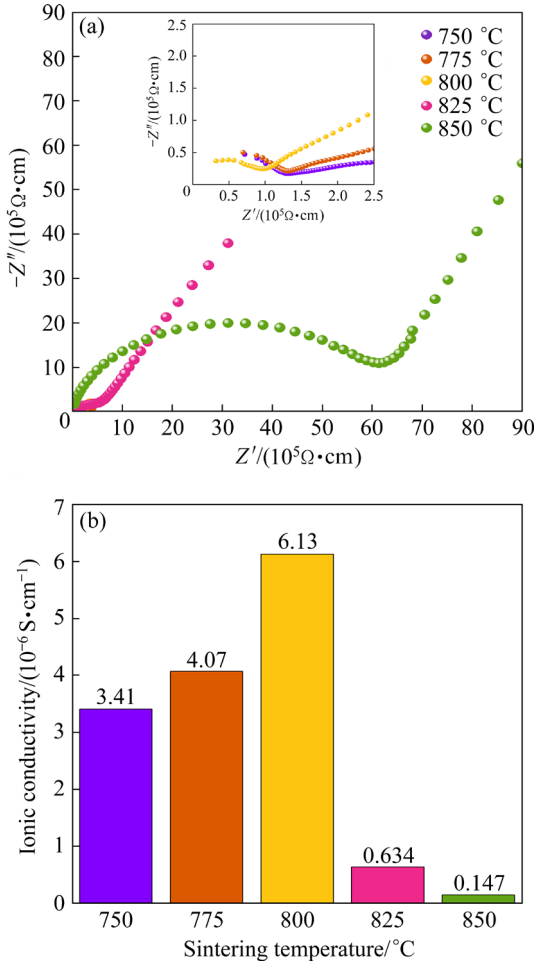


**Fig. 11** Impedance spectra (a) and corresponding ionic conductivities (b) of Sample C3 after sintering at different temperatures

All in all, enhanced electrical conductivity can be achieved by introducing an appropriate amount of $Cr^{3+}$ into the NTP materials, and this effective improvement in electrical properties can be attributed to the multiple excellent effects of $Cr^{3+}$ on the NASICON-type structure. First, due to the substitution of the +4-valent metal cation $Ti^{4+}$ by low-valence $Cr^{3+}$, additional $Na^+$ is introduced to compensate for the charge, and the carrier concentration in the NPT matrix is thus increased. Secondly, the ontological structure can be optimized by the entry of larger radii of $Cr^{3+}$ into the lattice, so that three-dimensional ion channels favorable to $Na^+$ diffusion are formed. Third, through the addition of $Cr^{3+}$, the formation of non-conductive secondary phases is effectively suppressed, the close packing of grains is promoted, and the hindrance in the process of ion migration is greatly reduced by these changes.

## 4 Conclusions

(1) The doping of $Cr^{3+}$ can effectively inhibit the formation of the impurity phase $TiP_2O_7$ and broaden the ion migration channels, whereas excessive doping of $Cr^{3+}$ will generate nonconducting $CrPO_4$ and result in distorted lattice deformation.

(2) SEM results show that the density is effectively improved by the addition of Cr, and the sintering properties are also improved. When the $Cr^{3+}$ doping amount is 0.3, the packing density between crystal grains is the largest, and the hindering effect during ion conduction is favorably reduced by this optimized microstructure.

(3) The AC impedance test results show that the ionic conductivity of the $Na_{1+x}Ti_{2-x}Cr_x(PO_4)_3$ system tends to increase and then decrease with the increase of $Cr^{3+}$ doping. The best room temperature ionic conductivity of $6.13\times10^{-6}$ S/cm is obtained at $x = 0.3$, which is 8 times that of the pure $NaTi_2(PO_4)_3$.

(4) This work proves that the crystal structure and microscopic morphology of the $Na_{1+x}Ti_{2-x}Cr_x(PO_4)_3$ system are improved by $Cr^{3+}$ doping, which is beneficial to the improvement of electrical conductivity and can provide a meaningful reference for the development of advanced electrolytes in the future.

### CRediT authorship contribution statement

**Cheng-jian WEN:** Conceptualization, Data curation, Writing − Original draft; **Zhi-wei LUO:** Formal analysis, Funding acquisition, Investigation,

Methodology, Writing − Review & editing; **Xin-yu LIU**, **Ju-xia TONG**, **Pan HE** and **An-xian LU:** Writing − Review & editing.

## Declaration of competing interest

The authors declare that they have no known competing financial interests or personal relationships that could have appeared to influence the work reported in this paper.

## Acknowledgments

The research was financially supported by the National Natural Science Foundation of China (No. 51972344), and the Natural Science Foundation of Hunan Province, China (No. 2018JJ3646).

## References

[1] GUO Zhi-hao, LI Xin-hai, WANG Zhi-xing, GUO Hua-jun, PENG Wen-jie, HU Qi-yang, YAN Guo-chun, WANG Jie-xi. Empirical decay relationship between ionic conductivity and porosity of garnet type inorganic solid-state electrolytes [J]. Transactions of Nonferrous Metals Society of China, 2022, 32: 3362−3373.

[2] LI Chun-lei, ZENG Shuang-wei, WANG Peng, LI Zhao-juan, YANG Li, ZHAO Dong-ni, WANG Jie, LIU Hai-ning, LI Shi-you. Mechanism of aluminum corrosion in LiFSI-based electrolyte at elevated temperatures [J]. Transactions of Nonferrous Metals Society of China, 2021, 31: 1439−1451.

[3] SHAO Yuan-jun, ZHONG Gui-ming, LU Ya-xiang, LIU Li-lu, ZHAO Cheng-long, ZHANG Qiang-qiang, HU Yong-sheng, YANG Yong, CHEN Li-quan. A novel NASICON-based glass-ceramic composite electrolyte with enhanced Na-ion conductivity [J]. Energy Storage Materials, 2019, 23: 514−521.

[4] FERGUS J W. Ion transport in sodium ion conducting solid electrolytes [J]. Solid State Ionics 2012, 227: 102−112.

[5] MARTÍNEZ-CISNEROS C S, PANDIT B, ANTONELLI C, SANCHEZ J Y, LEVENFELD B, VAREZ A. Development of sodium hybrid quasi-solid electrolytes based on porous NASICON and ionic liquids [J]. Journal of the European Ceramic Society, 2021, 41: 7723−7733.

[6] TIAN Hao-qing, LIU Shan, DENG Li-jun, WANG Ling, DAI Lei. New-type Hf-based NASICON electrolyte for solid-state Na-ion batteries with superior long-cycling stability and rate capability [J]. Energy Storage Materials, 2021, 39: 232−238.

[7] LI Zhao-peng, LIU Pei, ZHU Kun-jie, ZHANG Zhao-yuan, SI Yu-chang, WANG Yi-jing, JIAO Li-fang. Solid-state electrolytes for sodium metal batteries [J]. Energy & Fuels, 2021, 35: 9063−9079.

[8] YANG Zhen-dong, TANG Bin, XIE Zhao-jun, ZHOU Zhen. NASICON-type $Na_3Zr_2Si_2PO_{12}$ solid-state electrolytes for sodium batteries [J]. ChemElectroChem, 2021, 8: 1035−1047.

[9] ANANTHARAMULU N, KOTESWARA-RAO K, RAMBABU G, VIJAYA-KUMAR B, RADHA V, VITHAL M. A wide-ranging review on Nasicon type materials [J]. Journal of Materials Science, 2011, 46: 2821−2837.

[10] GUIN M, TIETZ F. Survey of the transport properties of sodium superionic conductor materials for use in sodium batteries [J]. Journal of Power Sources, 2015, 273: 1056−1064.

[11] ZHU Dong-mei, LUO Fa, XIE Zhang-long, ZHOU Wan-cheng. Phase formation and electrical characteristic of NASICON ceramics [J]. Transactions of Nonferrous Metals Society of China, 2007, 17: 1156−1159.

[12] JIAN Ze-lang, HU Yong-sheng, JI Xiu-lei, CHEN Wen. NASICON-structured materials for energy storage [J]. Advanced Materials, 2017, 29: 1601925.

[13] NIETO-MUÑOZ A M, ORTIZ-MOSQUERA J F, RODRIGUES A C M. Novel sodium superionic conductor of the $Na_{1+x}Ti_2Si_xP_{3-x}O_{12}$ series for application as solid electrolyte [J]. Electrochimica Acta, 2019, 319: 922−932.

[14] NIETO-MUÑOZ A M, ORTIZ-MOSQUERA J F, RODRIGUES A C M. The role of $Al^{3+}$ on the micro-structural and electrical properties of $Na_{1+x}Al_xTi_{2-x}(PO_4)_3$ NASICON glass-ceramics [J]. Journal of Alloys and Compounds, 2020, 820: 153148.

[15] MOUAHID F E, BETTACH M, ZAHIR M, MALDONADO-MANSO P, BRUQUE S, LOSILLA E R, ARANDA M A G. Crystal chemistry and ion conductivity of the $Na_{1+x}Al_xTi_{2-x}(PO_4)_3$ $(0 \le x \le 0.9)$ NASICON series [J]. Journal of Materials Chemistry, 2000, 10: 2748−2757.

[16] LUO Zhi-wei, QIN Chun-chun, XU Wen-jing, LIANG Hao-zhang, LEI Wei-cheng, SHEN Xue-feng, LU An-xian. Crystal structure refinement, microstructure and ionic conductivity of $ATi_2(PO_4)_3$ (A=Li, Na, K) solid electrolytes [J]. Ceramics International, 2020, 46: 15613−15620.

[17] ZHANG Qi-chong, MAN Ping, HE Bing, LI Chao-wei, LI Qiu-long, PAN Zheng-hui, WANG Zhi-xun, YANG jiao, WANG Zhe, ZHOU Zhen-yu, LU Xi-hong, NIU Zhi-qiang, YAO Ya-gang, WEI Lei. Binder-free $NaTi_2(PO_4)_3$ anodes for high-performance coaxial-fiber aqueous rechargeable sodium-ion batteries [J]. Nano Energy, 2020, 67: 104212.

[18] KATLAKUNTA S, MEENA S S, SRINATH S, BOUOUDINA M, SANDHYA R, PRAVEENA K. Improved magnetic properties of $Cr^{3+}$ doped $SrFe_{12}O_{19}$ synthesized via microwave hydrothermal route [J]. Materials Research Bulletin, 2015, 63: 58−66.

[19] LAI Yuan-ming, LIANG Xiao-feng, YANG Shi-yuan, LIU Pei, ZENG Yi-ming, HU Chang-yi. Raman and FTIR spectra of $CeO_2$ and $Gd_2O_3$ in iron phosphate glasses [J]. Journal of Alloys and Compounds, 2014, 617: 597−601.

[20] LAI Yuan-ming, LIANG Xiao-feng, YANG Shi-yuan, WANG Jun-xia, CAO Lin-hong, DAI Bo. Raman and FTIR spectra of iron phosphate glasses containing cerium [J]. Journal of Molecular Structure, 2011, 992: 84−88.

[21] QIAN Bin, YANG Shi-yuan, LIANG Xiao-feng, LAI Yuan-ming, GAO Long, YIN Guang-fu. Structural and thermal properties of $La_2O_3$−$Fe_2O_3$−$P_2O_5$ glasses [J]. Journal of Molecular Structure, 2012, 1011: 153−157.

[22] SHI Mei-qing, LIANG Yan-jie, CHAI Li-yuan, MIN

Xiao-bo, ZHAO Zong-wen, YANG Shu. Raman and FTIR spectra of modified iron phosphate glasses containing arsenic [J]. Journal of Molecular Structure, 2015, 1081: 389−394.

[23] LU Ming-wei, WANG Fu, LIAO Qi-long, CHEN Kui-ru, QIN Jian-fa, PAN She-qi. FTIR spectra and thermal properties of $TiO_2$-doped iron phosphate glasses [J]. Journal of Molecular Structure, 2015, 1081: 187−192.

[24] RAO M K, BABU K V, VEERAIAH V, SAMATHA K. Effect of Nb substitution on structural, electrical and electrochemical properties of $LiTi_2(PO_4)_3$ as electrolyte materials for lithium ion batteries [J]. Journal of Asian Ceramic Societies, 2018, 6: 109−120.

[25] ORTIZ-MOSQUERA J F, NIETO-MUÑOZ A M, RODRIGUES A C M. Precursor glass stability, microstructure and ionic conductivity of glass-ceramics from the $Na_{1+x}Al_xGe_{2-x}(PO_4)_3$ NASICON series [J]. Journal of Non-Crystalline Solids, 2019, 513: 36−43.

[26] BRADTMÜLLER H, NIETO-MUÑOZ A M, ORTIZ-MOSQUERA J F, RODRIGUES A C M, ECKERT H. Glass-to-crystal transition in the NASICON glass-ceramic system $Na_{1+x}Al_xM_{2-x}(PO_4)_3$ (M=Ge, Ti) [J]. Journal of Non-Crystalline Solids, 2018, 489: 91−101.

# $Cr^{3+}$离子掺杂改善 NASICON 型 $NaTi_2(PO_4)_3$ 固态电解质的晶体结构与导电性能

温成健，罗志伟，刘新宇，童菊霞，何 盼，卢安贤

中南大学 材料科学与工程学院，长沙 410083

**摘 要：**采用固相反应法制备一系列 $Cr^{3+}$离子取代的 $Na_{1+x}Ti_{2-x}Cr_xP_3O_{12}$($x$ = 0.1, 0.2, 0.3, 0.4, 0.5，摩尔分数)固态电解质。通过 X 射线粉末衍射、场发射扫描电子显微镜和交流阻抗测试，研究 $Cr^{3+}$离子对钠基导体的相组成、显微组织和电化学离子电导率的影响。结果表明，在固体电解质中生成 $NaTi_2(PO_4)_3$ 的主晶相，15%(摩尔分数)的 $Cr^{3+}$离子取代 $Ti^{4+}$位有助于抑制杂相的形成及拓宽离子通道，并通过改善晶粒的粘结程度共同促进电导率的增强。$Na_{1.3}Ti_{1.7}Cr_{0.3}P_3O_{12}$ 电解质在室温下可获得 $6.13\times10^{-6}$ S/cm 最佳离子电导率，是未掺杂 $NaTi_2(PO_4)_3$ 电解质的 8 倍。

**关键词：**$NaTi_2(PO_4)_3$；固态电解质；晶体结构；离子电导率；Cr 掺杂

**(Edited by Xiang-qun LI)**